Energy & Environmental Science

Lithium Degradation in Lithium-Sulfur Batteries: Insights into Inventory Depletion and Interphasial Evolution with Cycling

Journal:	*Energy & Environmental Science*
Manuscript ID	EE-ART-04-2020-001074.R1
Article Type:	Paper
Date Submitted by the Author:	30-Jun-2020
Complete List of Authors:	Nanda, Sanjay; University of Texas at Austin Manthiram, Arumugam; University of Texas at Austin, Materials Science and Engineering

Energy and Environmental Science

PAPER

Lithium Degradation in Lithium-Sulfur Batteries: Insights into Inventory Depletion and Interphasial Evolution with Cycling

Sanjay Nanda[a] and Arumugam Manthiram*[a]

Received 00th January 20xx,
Accepted 00th January 20xx

DOI: 10.1039/x0xx00000x

The promise of high energy density lithium-sulfur batteries with long cycle life is currently tempered by the rapid degradation of lithium-metal anodes with cycling. An in-depth understanding of its dynamical behavior in liquid electrolytes, including the mechanisms underlying depletion of lithium inventory and evolution of lithium interphases, is crucial to make Li-S batteries a reality. We use here an anode-free full cell configuration, pairing a Li_2S cathode with a bare nickel current collector with no lithium metal on it, to quantitatively estimate the lithium inventory loss per cycle. Lithium inventory loss is shown to be the main factor limiting the overall cyclability of Li-S batteries. Time-of-flight secondary ion mass spectrometry measurements on the deposited lithium reveal the presence of substantial metallic lithium even after most of the active lithium inventory has been depleted. The trapped metallic lithium is rendered electrochemically inactive by the growth of a resistive electrolyte decomposition interphase on the lithium surface. The bulk of the deposited lithium is shown to be composed of various fully reduced interphasial components, including several hydrogen-containing species that show a substantial reduction in intensity with cycling. This indicates considerable gas evolution and is also correlated with the loss of lithium inventory. The use of an anode-free full cell configuration provides a framework for accurate assessment of the dynamics of lithium inventory depletion and characterization of the accompanying interphasial evolution with cycling. The insights gained will prove invaluable to the development of strategies for extending the cycle life of energy-dense Li-S batteries.

Broader context

The lithium-sulfur couple is widely considered as one of the most promising battery chemistries for the next generation of energy storage technologies. While considerable progress has been made on resolving the numerous issues with sulfur cathodes, further development is still limited by the rapid degradation of lithium-metal anodes with cycling. The poor reversibility of plating and stripping lithium limits the cycle life of practically relevant Li-S batteries constrained by a limited lithium inventory. A clear picture of the dynamics of lithium inventory depletion and accompanying interphasial evolution in Li-S batteries is necessary for developing strategies towards improving lithium cycling efficiency. In this work, we use an anode-free full cell configuration, which has a limited lithium inventory, to provide a quantitative description of lithium inventory loss rate per cycle. The depletion of lithium inventory with cycling is found to be correlated with the growth of an electrolyte decomposition interphase on lithium surface, which renders the metallic lithium underneath electrochemically inactive. Hence, lithium degradation in Li-S batteries is precipitated by the formation of metallic "dead" lithium as opposed to the consumption of active lithium in parasitic side reactions. Evidence also points to substantial gas evolution in the course of cycling, which can play a role in inducing failure of lithium anodes. This work provides a framework for understanding lithium deposition in Li-S batteries and sheds light on the dynamically evolving lithium interphases. The insights generated in this work are expected to spur further development towards advanced Li-S batteries with high energy density and long cycle life.

1 Introduction

The development of energy-dense, efficient, and economical electrical energy storage (EES) technologies is critical to the widespread adoption of all-electric transportation and renewable power sources. Rechargeable lithium-sulfur (Li-S) batteries are one of the most promising candidates for realizing the next generation of this keystone technology.[1,2] In contrast to the transition-metals in Li-ion batteries, sulfur is inexpensive, non-toxic, and widely available. Despite its lower voltage output (2.1 V), it has a high theoretical gravimetric capacity of 1,675 mA h g^{-1}, which is more than 10 times that of incumbent cobalt-oxide cathodes. However, sulfur cathodes suffer from many intrinsic challenges, including poor conductivity, volume expansion, and dissolution of polysulfide intermediates. Over the last decade, there have been sustained attempts from researchers all over the world towards solving these issues. With highly optimized cathode architectures, which incorporate porous, conductive, and polysulfide-trapping host materials, excellent cyclability (> 1,000 cycles) has been demonstrated.[3,4] However, these demonstrations have been

[a] Materials Science and Engineering Program & Texas Materials Institute
The University of Texas at Austin, Austin, TX 78712, USA
manth@austin.utexas.edu

†Electronic supplementary Information available: See DOI: 10.1039/x0xx00000x

typically under unrealistic testing conditions – low sulfur loadings (< 2 mg cm^{-2}), flooded electrolyte cells, and thick lithium-foil anodes. With high sulfur loadings, lean-electrolyte, and controlled lithium amount, the cyclability is much more limited. There is a need for concerted efforts to achieve reasonable cyclability without compromising on energy density to realize their commercial potential of Li-S batteries.[5–7]

One of the major and relatively under-investigated bottlenecks to achieving good cyclability in Li-S batteries under realistic cell design conditions is the lithium-metal anode. Theoretically, lithium metal is the ideal anode material due to its low reduction potential (-3.01 V vs SHE) and high gravimetric capacity (3,861 mA h g^{-1}).[8,9] Practically, however, the poor efficiency of plating and stripping lithium remains an intractable issue. At reasonable current densities and in the ether-based liquid electrolyte, the deposition of lithium undergoes a mossy growth regime, in which lithium deposits with a porous filamentous morphology and a large surface area are formed.[10] Owing to the low reduction potential of lithium, severe parasitic side reactions with the electrolyte are engendered, which leads to an irreversible loss of both lithium and electrolyte supply in the cell. This limits the achievable Coulombic efficiencies of lithium plating/stripping, which are generally quite low (< 99%) in unoptimized systems. Stable cycling can be artificially realized by employing excess lithium and electrolyte, but this obviates the energy density advantage of Li-S batteries.[11,12] Furthermore, electrolyte depletion at the lithium interface can lead to lithium deposition under the diffusion-limited dendritic growth regime, which may be accentuated by localized high current densities. The lithium dendrites formed can pierce the separator and short the cell internally, causing major safety issues.[13–15] Hence, one of the major goals for further development of Li-S batteries is stabilizing lithium deposition and improving the reversibility and safety of lithium-metal anodes.

Designing effective strategies towards achieving this goal necessitates developing a thorough understanding of the role and dynamical behaviour of the lithium-metal anode in Li-S batteries. However, a detailed picture of the mechanisms underlying lithium degradation in the polysulfide-rich electrolyte is still lacking. One of the main reasons for this is the absence of a suitable framework for accurately evaluating lithium deposition in Li-S batteries. The ubiquitous Li || S half cells, which pair sulfur cathodes with lithium-metal foil anodes, typically contain a large excess of lithium (Li/S capacity ratio > 10) and reveal no useful information on lithium deposition in such systems.[16,17] The electrochemical performance of Li || S half cells is entirely representative of the sulfur cathode. Using thin lithium foils to reduce the amount of excess lithium can be more instructive, but nevertheless it is non-trivial to control the Li/S capacity ratio and deconvolute the impact of irreversible lithium deposition on overall electrochemical performance. Even Li || Cu half cells, which are widely employed to obtain Coulombic efficiencies of lithium plating/stripping, are inadequate for reliably modelling lithium deposition in Li-S batteries.[18–20] The dynamically varying concentration and composition of polysulfide intermediates in the electrolyte of a real Li-S battery cannot be replicated by using polysulfides as electrolyte additives.[21] Hence, a new framework is needed for achieving truly lithium-limited electrochemical performance in Li-S batteries and effectively investigating the dynamics of lithium degradation in such systems.

The characteristics of lithium deposition are closely affected by the solid-electrolyte interphase (SEI) layer, which is formed by the decomposition of the electrolyte on the lithium surface.[22,23] Various properties of the SEI layer, such as Li^+-ion conductivity, electronic resistivity, interfacial energy, mechanical robustness, and chemical passivation are critical to determining the efficiency of lithium plating and stripping.[24–26] Since lithium metal is a "hostless" anode and is accompanied by large volume changes, the SEI layer is not a stable interface and undergoes substantial reconstruction in the course of cycling.[27,28] Furthermore, lithium deposition in Li-S batteries is uniquely impacted by the presence of polysulfide intermediates, which exist in a dynamic equilibrium with their reduction products, Li_2S and Li_2S_2, on lithium surface.[29,30] Despite a number of excellent work that have attempted to shed light on the unique SEI layer in Li-S batteries, which have been reviewed by Cheng et. al., a number of ambiguities remain.[31–33] In particular, the changes in the composition of the interphase formed on the deposited lithium as it degrades with cycling remain unclear. Stabilizing lithium deposition in Li-S batteries requires developing an accurate picture of the mechanisms underlying lithium degradation and the role of the dynamically evolving interphase on the lithium surface.

In this work, we use an anode-free Ni || Li_2S full cell configuration, which pairs a Li_2S cathode with a bare Ni foil with no lithium on it, to provide a robust and reliable evaluation of lithium deposition in Li-S batteries.[34–36] Since there is no excess lithium and the Li/S capacity ratio is exactly controlled at 1 as in lithium-ion cells, the electrochemical performance of the anode-free system is limited by the efficiency of lithium plating and stripping. This allows, for the first time, a quantitative description of lithium degradation, and specifically, the depletion of electrochemically active lithium metal with cycling. The deposited lithium in the anode-free full cells after different cycle numbers was analyzed by time-of-flight secondary ion mass spectrometry (ToF-SIMS). It is revealed that the loss of cyclable lithium is not due to the consumption of lithium in parasitic side reactions with the electrolyte, but due to the entrapment of metallic "dead" lithium by a thick resistive layer of electrolyte decomposition products that grows with cycling. The loss of cyclable lithium is found to be accompanied by the disappearance of hydrogen-containing interphasial components in the bulk of the deposited lithium, which is likely engendered by the generation of H_2 and other hydrocarbon gases during cycling. The deposited lithium is also progressively enriched with Li_2S due to extended polysulfide reduction with cycling. A combination of gas evolution and Li_2S formation is expected to further limit the electrochemical accessibility to the trapped metallic lithium. We believe this approach represents an important step forward towards developing an effective framework for quantitatively evaluating lithium inventory depletion, as well as understanding the interphasial evolution underlying lithium degradation in Li-S batteries.

2 Experimental

2.1 Li_2S Cathode Preparation

Commercial lithium sulfide (Li_2S, Alfa Aesar) was combined with commercial multi-walled carbon nanotubes (MWCNT, NanoAmor) in a 4 : 1 ratio by weight. The mixture was dry ball-milled using zirconia (YSZ) grinding media in a zirconia milling vessel with a planetary ball-milling system. The milling duration was 15 iterations of 30 minutes of milling followed by 30 minutes of rest. The resulting Li_2S/MWCNT composite was further wet ball-milled with 1,3-dioxolane / 1,2-dimethoxyethane (DOL/DME, 1:1 vol.) as the slurry medium in a 1 : 20 ratio by weight. The wet milling was conducted in a PTFE bottle with the previously used zirconia grinding media for 24 hours using a long roll jar-milling system. The resulting slurry was drop-cast between two pieces of carbon paper of diameter 11.1 mm and allowed to dry in the glove box ambient. Free-standing, binder-free cathodes with a final Li_2S loading of 4 mg cm^{-2} of Li_2S and a Li_2S content of 45% were obtained.

2.2 Electrochemical Measurements

Anode-free full cells with the configuration Ni || Li_2S and half cells with the configuration Li || Li_2S were assembled in the CR2032 coin cell format. Nickel foils of diameter 14.3 mm were used as the anode current collector without any modifications or pre-treatments in the full cells. Lithium foils of thickness 0.6 mm and diameter 14.3 mm were used in the half cells. Two pieces of Celgard 2500 were used as the separator. A thrice-folded nickel foam of diameter 7.9 mm was used as the spacer. The electrolyte used was the standard 1 M lithium bis(trifluoromethanesulfonyl)imide (LiTFSI) + 0.1 M $LiNO_3$ in DOL/DME (1 : 1 vol). The electrolyte amount was controlled at 120 µl. The cells were rested for 12 hours before galvanostatic cycling at C/10 (~ 0.5 mA cm^{-2}) or C/5 (~ 1 mA cm^{-2}) current rates with a 2.8 V – 1.8 V voltage window. The initial charge step was conducted at C/20 rate with a voltage limit of 4 V or a time limit of 20 h in all cases.

2.3 Materials Characterization

The deposited lithium in the anode-free full cells was characterized with X-ray photoelectron spectroscopy (XPS) and time-of-flight secondary ion mass spectrometry (ToF-SIMS). The Ni foils with the deposited lithium were retrieved after cell disassembly and carefully washed with blank DOL/DME cosolvent to remove any soluble products, such as polysulfides and unreacted LiTFSI on the surface. XPS measurements were conducted with a Kratos Axis Ultra DLD Spectrometer. ToF-SIMS measurements were conducted with an ION-TOF TOF.SIMS 5 spectrometer. A custom-built air and moisture-sensitive stainless-steel chamber was used for transferring the samples to the XPS and ToF-SIMS measurement chambers. XPS spectra were collected with a monochromatic aluminum Kα source of energy 1468.5 eV tuned at 12 kV and 10 mA. The pass energy was set as 20 eV with an energy step of 0.1 eV. The ToF-SIMS measurements were conducted in the negative mode. A 2 keV Cs^+ ion beam was used to sputter the deposited lithium and generate the secondary ions. A pulsed 30 keV Bi^+ ion beam was used in the high current mode for depth profiling. The sputtering area and analysis area were, respectively, 300 x 300 $\mu m^2$and 100 x 100 μm^2.

3 Results and Discussion

3.1 Lithium Inventory Depletion in Li-S Batteries

The anode-free full cell configuration, which pairs the fully lithiated Li_2S cathode with a plain nickel foil current collector on the anode side, is used to investigate the dynamics of lithium deposition in this study. The Li/S capacity ratio in the anode-free full cells is precisely equal to 1 by design. In this work, the anode-free Ni || Li_2S full cell uses 4 mg cm^{-2} of Li_2S, which corresponds to a theoretical capacity of 4.66 mAh cm^{-2} for both sulfur and lithium. In contrast, an equivalent Li || Li_2S half cell employing a 600 µm thick lithium foil has a theoretical capacity of 4.66 mAh cm^{-2} for sulfur and 128.37 mAh cm^{-2} for lithium, which correspond to an Li-S capacity ratio of 27.5. Lean-electrolyte conditions were not employed to avoid convoluting the results with the additional variable of low E/S ratio. The large excess of lithium effectively behaves as a lithium reservoir from which any lithium lost to inefficiencies in the plating and stripping process can be recovered. Assuming complete replenishment of lithium losses, the measured capacity of a Li || Li_2S half cell at any given cycle is simply the sulfur inventory that is still electrochemically active. Due to the complete absence of any excess lithium in the anode-free system, any losses in lithium inventory are irreversible and lead to a corresponding loss in capacity. Hence, the measured capacity of an anode-free Ni || Li_2S full cell at any given cycle is simply the smaller of the active lithium inventory and active sulfur inventory. Comparing the electrochemical performance of both cell configurations allows a quantitative evaluation of lithium and sulfur inventory loss in the Li-S system. Fig. 1a illustrates the main differences between the two cell configurations.

Fig. 1b and Fig. 1c show the measured discharge capacity as a function of cycle number for Li || Li_2S half cells and anode-free Ni || Li_2S full cells at C/10 (~ 0.5 mA cm^{-2}) and C/5 (~ 1 mA cm^{-2}) current rates. Capacity retention is reported as a percentage of the theoretical capacity (1,165 mAh g^{-1}, 4.66 mAh cm^{-2}) and all gravimetric capacities are reported with respect to the weight of Li_2S in the cathode. At C/10 rate, the Li || Li_2S half cell shows a first-cycle discharge capacity of 3.25 mAh cm^{-2} (813 mAh g^{-1}, 70% retention) and a fifth-cycle discharge capacity of 2.5 mAh cm^{-2} (54% retention). In subsequent cycles, the capacity fade is much more muted. The anode-free Ni || Li_2S full cell shows similar initial capacities as the half cell, with a first cycle discharge capacity of 3.14 mAh cm^{-2} (783 mAh g^{-1}, 68% retention) and a fifth-cycle discharge capacity of 2.4 mAh cm^{-2} (52% retention). Subsequently, the anode-free full cell shows a very similar capacity fade profile as the half cell, retaining 2 mAh cm^{-2} of discharge capacity at 80 cycles, compared to 2.1 mAh cm^{-2} for the half cell. After 80 cycles, however, the capacity fade profiles diverge significantly. The discharge capacity of the anode-free full cell declines rapidly to 1 mAh cm^{-2} (22% retention) at 200 cycles, while the half cell maintains 1.7 mAh cm^{-2} (36% retention). A comparable trend can also be observed at C/5 rate. The anode-free full cell and half cell show similar capacities initially, with a peak capacity of 2.65 mAh cm^{-2} (658 mAh g^{-1}, 57% retention) for the full cell and 2.8 mAh cm^{-2} (711 mAh g^{-1}, 61% retention) for the half cell. At 25 cycles, the anode-free full cell maintains a capacity of 2.15 mAh cm^{-2} (46% retention), while the half cell maintains a capacity of 2.2 mAh cm^{-2} (47% retention). The capacity fade profiles diverge sharply after 25 cycles, and the anode-free full cell only retains 0.8 mAh cm^{-}

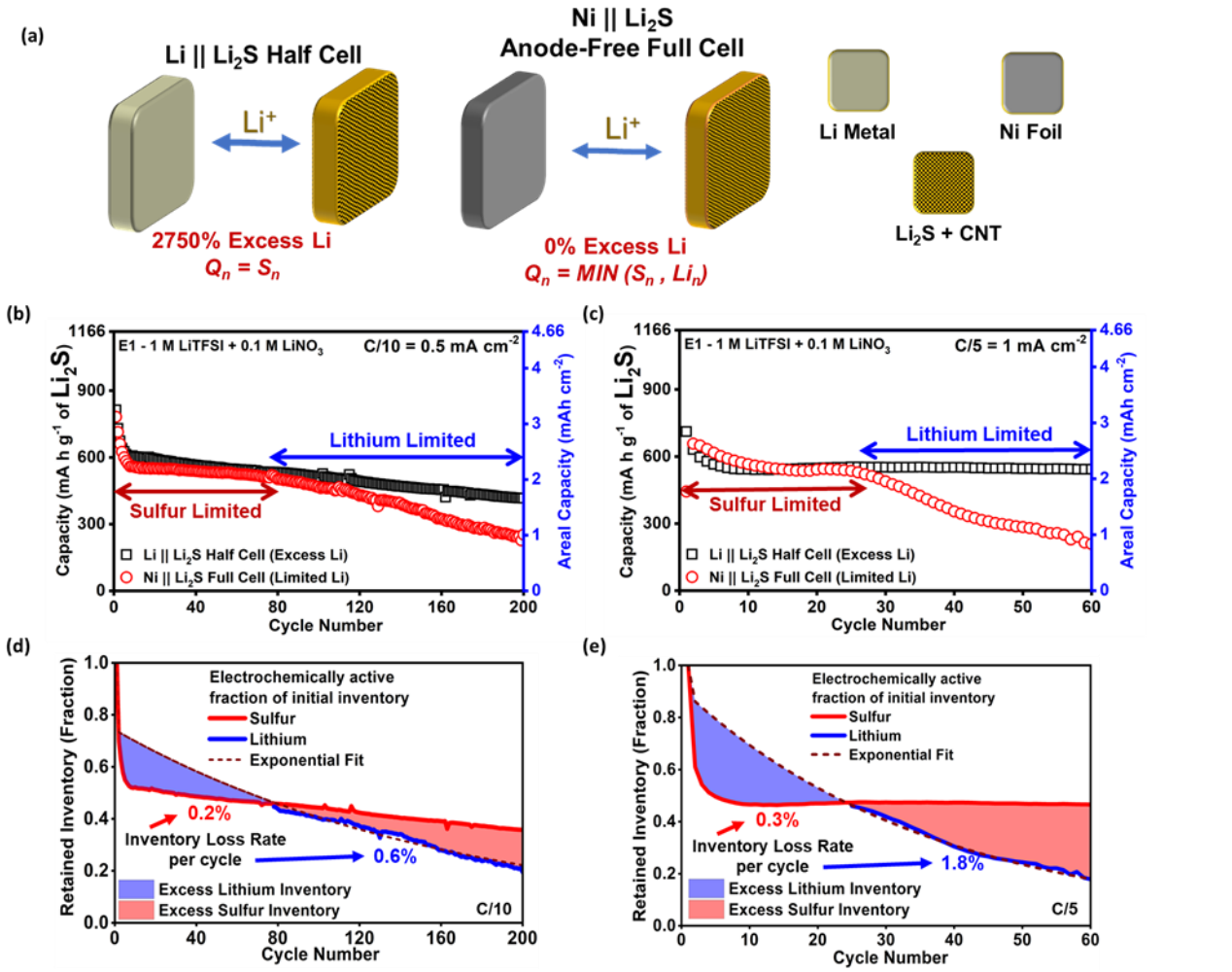

Fig. 1. (a) Schematic illustration of a Li || Li_2S half cell with 2,750% excess lithium, whose measured discharge capacity Q_n, for any cycle number n, is simply the active sulfur inventory in the system S_n. For an anode-free Ni || Li_2S full cell with no excess lithium, the measured capacity Q_n at cycle number n is the smaller of the active lithium inventory (Li_n) and active sulfur inventory (S_n); electrochemical performance of Li || Li_2S half cell and anode-free Ni || Li_2S full cell at (b) C/10 = 0.5 mA cm^{-2} and (c) C/5 = 1 mA cm^{-2} rates, clearly showing two different cycling regimes, with initial capacity fade corresponding to lithium excess and subsequent capacity fade corresponding to sulfur excess; fraction of sulfur and lithium inventory retained as a function of cycle number at (d) C/10 and (e) C/5 rates. Lithium inventory retention is fitted with an exponential function, which allows extrapolation to the initial sulfur-limited cycling regime and estimation of inventory loss rates. The doubling of C-rate increases the lithium inventory loss rate from 0.6% to 1.8% per cycle.

^{2} (17% retention) at 60 cycles, while the half cell still maintains 2.2 mAh cm^{-2} (47% retention). Thus, the anode-free full cell shows two distinct cycling regimes, where it initially traces the slow capacity fade of the half cell before transitioning into rapid capacity loss. The transition between the two regimes occurs at 80 cycles for C/10 rate and at 25 cycles for C/5 rate. Cycling data up to 200 cycles for the anode-free Ni || Li_2S full cell at C/5 rate is shown in Fig. S1. Fig. S2 shows the charge/discharge curves and the increase in polarization accompanying the cycling of the Li || Li_2S half cell and anode-free Ni || Li_2S full cell at both C/10 and C/5 rates.

Since the Li || Li_2S half cells have a large excess of lithium, their measured discharge capacities can be considered equal to the active sulfur inventory in the system. Furthermore, since the only difference between the half cells and the anode-free full cells is the amount of excess lithium present, the active sulfur inventory as a function of cycle number should be nominally equal in both systems. In the second cycling regime of anode-free Ni || Li_2S full cells, when its electrochemical performance diverges from half cells and shows rapid capacity fade, the measured discharge capacities can be considered equal to the active lithium inventory in the system. The fraction of sulfur and lithium inventory retained versus cycle number in these example Li-S systems is shown in Fig. 1d for C/10 rate and Fig. 1e for C/5 rate. Thus, the rapid capacity fade in the second cycling regime can be attributed to the rapid loss of lithium inventory, which is more depleted compared to sulfur inventory in this "lithium-limited" regime. Prior to the transition point, the slow capacity fade in the first cycling regime can be attributed to the slow loss of sulfur inventory, which is more depleted compared to lithium inventory in this "sulfur-limited" regime. This is engendered when the loss of sulfur inventory in the initial ~ 5 cycles is higher compared to the loss of lithium inventory over the same period. In these example Li-S systems, ~ 50% of the initial sulfur inventory is lost over the first five cycles. This creates *in-situ* a slight excess of lithium inventory in the anode-free full cells, due to which they show similar behaviour as the half cells in the first cycling regime. However, since the depletion of lithium inventory is much faster compared to that for sulfur, this slight excess of lithium gets fully depleted. A transition point between the two cycling regimes is reached, when the active lithium inventory reaches parity with the active sulfur inventory.

Subsequently, rapid capacity fade is observed in accordance with the rapid depletion of lithium inventory.

The fraction of lithium inventory retained in the second cycling regime, as shown in Fig. 1d and 1e, can be fit with an exponential function, using the following formula

$$\boldsymbol{Q_n = Q_t * (1 - LILR/100)^{t-n}} \quad (1)$$

where Q_n is the capacity after n cycles, Q_t is the capacity at the transition point (cycle number = t) and *LILR*, or lithium inventory loss rate, is an averaged percentage loss of lithium inventory per cycle. While actual inventory losses show significant cycle-to-cycle variations, the average LILR value obtained using the exponential fit is nevertheless convenient for comparison across different cases. At C/10 rate, the LILR is found to be 0.6% per cycle, while it increases to 1.8% per cycle at C/5 rate. Sulfur inventory loss rates can also be calculated in the first cycling regime by a method analogous to that for LILR. It is found to be 0.2% per cycle at C/10 rate and 0.3% per cycle at C/5 rate. The exponential fits were extrapolated to before the transition point to illustrate the slight excess of lithium inventory in the first cycling regime and its eventual depletion. When extrapolated all the way to the first cycle, it can be seen that the difference in initial inventory losses between sulfur (~ 50%) and lithium (< 25%) is responsible for the slight excess of lithium inventory, which causes the "capacity plateau" observed in the first cycling regime. Moreover, it can be seen that the faster loss of lithium inventory at C/5 rate (1.8% per cycle) leads to the transition point reached earlier at 25 cycles, compared to C/10 rate (0.6% per cycle) where the transition point is reached at 80 cycles.

The quantitative estimation of lithium inventory loss rate using the anode-free full cell configuration provides a robust and effective framework for evaluating the dynamics of lithium deposition. This applies not just to Li-S batteries, but to lithium-metal batteries generally. The traditional parameters for evaluating lithium deposition, **i.e.**, plating/stripping overpotentials in Li || Li symmetric cells or Coulombic efficiencies in Li || Cu half cells, only provide an incomplete description as they do not correlate directly with the loss of lithium inventory in practically relevant lithium-limited systems. They also do not account for the role played by the cathode, which is particularly important for systems with considerable active material dissolution, such as sulfur and NMC layered oxides.[37–40] Furthermore, the values of Coulombic efficiencies registered during cycling are not always a perfect predictor of capacity fade, especially in systems with an internal redox shuttle.[41,42] This applies to the anode-free full cells described in this work, and a brief discussion follows in the Supporting Information (Fig. S3). The lithium inventory loss rate, as calculated using the lithium-limited cycling regime of an anode-free full cell, although nominally analogous to the Coulombic inefficiency, provides the most comprehensive description of lithium deposition in a lithium-limited system. For a given applied current density and initial plating capacity, it can be used to accurately predict cycle life with a limited lithium inventory. It can also be used to achieve a reliable and quantitative comparison of lithium degradation across different lithium-limited systems.

Three important conclusions can be derived from the results discussed above. First, even at the relatively low current density of 0.5 mA cm^{-2}, lithium inventory loss (0.6% per cycle) is more severe compared to that for sulfur (0.2% per cycle), and is the main factor limiting long-term cyclability of Li-S batteries. Second, at the elevated current density of 1 mA cm^{-2}, while sulfur inventory loss is only slightly increased to 0.3% per cycle, lithium inventory loss is much more aggravated and increases to 1.8% per cycle. Hence, further efforts at improving the cyclability of Li-S batteries at reasonable current rates should be focused on improving the efficiencies of lithium plating/stripping and use the anode-free full cell configuration for validation. Third, initial losses of sulfur inventory can be quite significant and may help conceal some of the limitations with the lithium anode. While improving sulfur utilization would not enhance the cyclability of Li-S batteries, it is necessary for delivering the maximum energy density from the system.

3.2 Mechanisms Underlying Lithium Inventory Depletion

Since anode-free full cells are assembled without any free lithium metal, the deposited lithium is entirely formed *in-situ* in the course of cycling. This makes it an ideal template for characterization of the interphasial evolution accompanying lithium degradation. The results are not skewed by the excess metallic lithium or the native passivation layer present in lithium metal foils. Hence, in order to understand the mechanisms underlying lithium degradation in Li-S batteries, the deposited lithium in the anode-free Ni || Li_2S full cells was analysed by time-of-flight secondary ion mass spectrometry (ToF-SIMS). ToF-SIMS is an ultrasensitive technique for obtaining compositional depth profiles for a sample that involves sputtering with a focused primary ion beam and characterizing the ejected secondary ions using mass spectrometry. The ejected secondary ions are fragments of the detected molecules, and hence indicate at least some degree of chemical bonding between the different atoms in the secondary ion.[43] The intensity for various secondary ions can also be integrated over the sputtered depth to obtain a high-resolution mass spectrum.

The deposited lithium was characterized after the charge step in the 5th, 40th, and 300th cycle at C/10 rate. While the 5th and 40th cycles belong to the stable first cycling regime, the 300th cycle corresponds to cell failure when most of the capacity has been lost. The ToF-SIMS measurements are carried out over a sample volume of 100 µm x 100 µm sputtering area times ~ 10 µm sputtered depth, assuming standard rates of sputtering for a lithium surface. Since this sampled volume is invariant, the integrated intensity for a secondary ion can be accurately compared across different samples. Fig. 2a shows the integrated intensity for Li_2^- secondary ion, which is representative of metallic lithium, for the different cycle numbers. In order to account for matrix effects, the intensities were scaled with respect to the total count of all secondary ions registered throughout the sampled depth.[44] It can be seen that the signal for metallic lithium does not show a significant difference with cycling, with a small decrease from 5th to 40th cycle and little change thereafter. Fig. 2b shows the expected active lithium inventory in the anode-free Ni || Li_2S full cell after 5, 40, and 300 cycles, as calculated based on the equation described previously. While a small change in lithium inventory is expected from 5 to 40 cycles, the majority of lithium inventory is expected to be depleted by the 300th cycle. Fig. 2c shows both the fraction of lithium inventory retained and the fraction of metallic lithium detected using ToF-SIMS, normalized to the values for the 5th cycle. The transition from 5 to 40 cycles brings about a slight

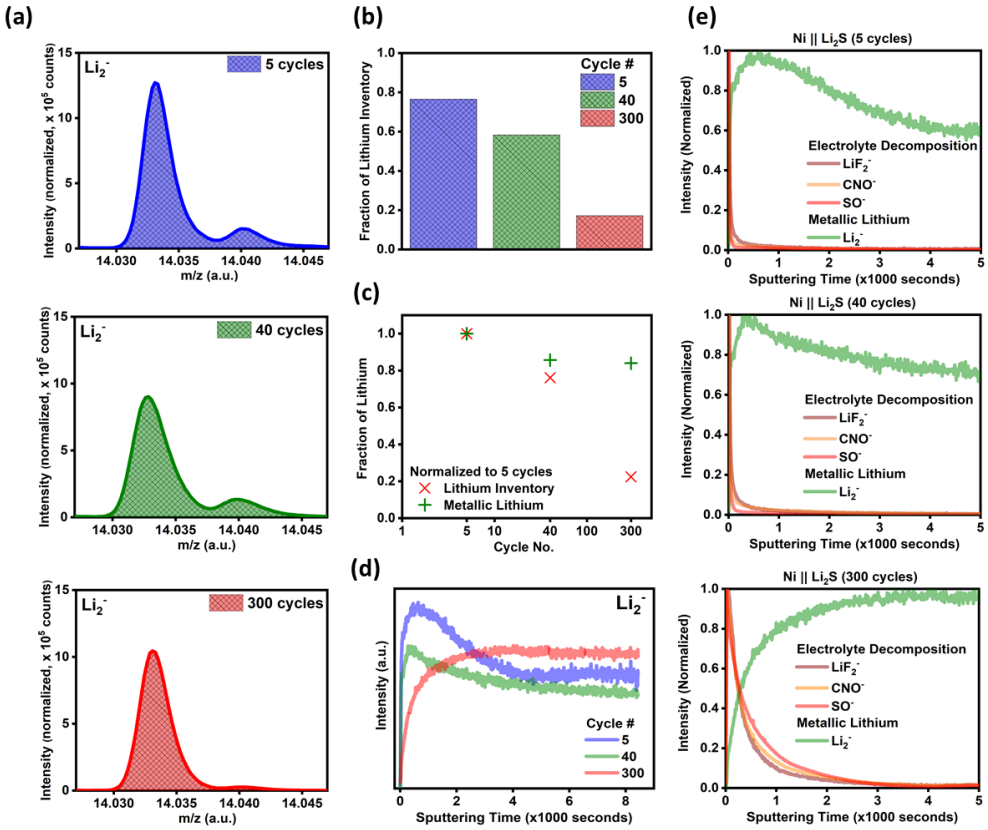

Fig. 2. (a) Integrated intensity of Li_2^- secondary ions obtained with ToF-SIMS for the deposited lithium in anode-free Ni || Li_2S full cells (cycled at C/10 rate) at 5, 40, and 300 cycles. The integrated intensity for Li_2^- is indicative of the amount of metallic lithium detected. A significant amount of metallic lithium can be detected at 300 cycles, even as most of the initial lithium inventory is depleted. This is demonstrated in (b), which shows the lithium inventory retained at 5, 40, and 300 cycles based on Equation (1). (c) Fraction of lithium inventory and detected metallic lithium in the 40th and 300th cycle as a fraction of that in the 5th cycle, showing the wide divergence in both that occurs with cycling. (d) Depth profiles for Li_2^- secondary ions as a function of sputtering time at 5, 40, and 300 cycles. (e) Depth profiles for Li_2^- secondary ions, indicative of metallic lithium, and LiF_2^-, CNO^-, and SO^- secondary ions, indicative of electrolyte salt decomposition products, at 5, 40, and 300 cycles. The depth profiles are normalized to the peak intensity for each secondary ion. The formation and growth of an electrolyte decomposition layer on the metallic lithium surface can be observed with cycling. By 300 cycles, metallic lithium is rendered electrochemically inactive or "dead" by the formation of a thick layer of electrolyte decomposition products, which leads to the loss of active lithium inventory.

reduction in both lithium inventory and detected metallic lithium. However, the transition from 40 to 300 cycles does not bring about any decrease in the detected signal for metallic lithium, despite a large decrease in the retained lithium inventory.

The presence of a significant amount of metallic lithium even as most of the cyclable lithium inventory has been depleted suggests that the dominant mechanism of lithium inventory loss in Li-S batteries is not irreversible side reactions with the electrolyte to form lithium compounds (Li^+) as SEI components, but the formation of electrochemically inaccessible "dead" metallic lithium (Li^0). While not a precise quantitative result due to the relatively small volume sampled with ToF-SIMS, this confirms the conclusion of a recent work by Fang et. al. about the mechanisms governing inactive lithium formation when cycling lithium-metal anodes.[45] Fig. 2d shows the depth profiles for Li_2^- secondary ions at cycle numbers 5, 40, and 300 as a function of sputtering time. As before, the measured signal is normalized with respect to the total signal for all secondary ions to eliminate matrix effects. Assuming a typical sputter rate of 1 nm s^{-1} for a 2 kV Cs^+ primary ion beam, the total sputtered depth is expected to be around 10 µm.[46,47] At 5 cycles, the signal for Li_2^- shows a sharp initial peak, but subsequently quickly declines to reach a steady value with increasing depth. At 40 cycles, the signal for Li_2^- shows a subdued initial peak and subsequently reaches a similar steady signal intensity. At 300 cycles, the signal for Li_2^- shows no initial peak whatsoever, but instead a slow increase to a steady signal intensity in the depth of the deposited lithium. The decrease and eventual disappearance of the initial peak for Li_2^- with cycling suggests the build-up of a SEI layer consisting of lithium-electrolyte reaction products on top of the deposited metallic lithium. Fig. S5 and S6 show that the conclusions derived in this section hold irrespective of whether normalization is applied to the ToF-SIMS data. It should also be noted here that while Li_3^- is also an indicator of metallic lithium, its integrated intensity and depth profiles show a similar relative trend as Li_2^- at 5, 40, and 300 cycles (Fig. S6). In this work, Li_2^- is chosen for the analysis due to its larger signal to noise ratio.

Fig. 2e compares depth profiles for secondary ions corresponding to various electrolyte decomposition products – SO^-, LiF_2^-, and CNO^- - with that for metallic lithium (Li_2^-) at 5, 40, and 300 cycles.[48] For easier comparison, the depth profiles for the different secondary ions are scaled from 0 to 1 with respect to the maximum signal intensity. The various electrolyte salt decomposition products are found to be concentrated on the surface, with their signals rapidly declining to zero in the bulk of the deposited lithium. By 300 cycles, the thickness of the electrolyte decomposition layer grows dramatically, with 10% of the peak signal intensity for SO^- reached after 40, 50, and 1130 seconds of sputtering at 5, 40, and 300 cycles

respectively. At 300 cycles, the signals for the various electrolyte decomposition products form an almost exact inverse of the signal for Li_2^-, which shows a gradual increase to a uniform value with increasing depth. This confirms that the deposited metallic lithium gets covered with a thick layer of electrolyte salt decomposition products with cycling. With increasing thickness of the SEI layer, electronic and ionic access to the trapped metallic lithium is impeded, which renders it electrochemically inactive or "dead". This is the main cause of lithium inventory loss in Li-S batteries. This also explains why a monotonic capacity fade is not observed with the Ni || Li_2S full cells in their second cycling regime (Fig. 1b). Since the plating and stripping of lithium is accompanied by large volume changes, the electrolyte decomposition layer is subject to considerable mechanical strain. If the ion-blocking SEI layer is fractured at any given site, some of the trapped lithium can temporarily become electrochemically available. This would lead to a small increase in the registered capacity, which is observed in the cycling of anode-free full cells.

3.3 Evolution of Interphases in Deposited Lithium

The deposited lithium in the anode-free Ni || Li_2S full cells was also analyzed by XPS. Unlike ToF-SIMS, XPS only analyses a depth of ~ 10 nm from the top surface of the sample. Fig. 3a shows the S 2p spectra for the surface of the deposited lithium after different cycle numbers with similar intensity (y-axis) scales. After 5 cycles, the lithium interphase is dominated by reduced sulfur species (Li_2S = 159.8 eV/Li_2S_2 = 161.3 eV), which are formed by polysulfide (Li_2S_n) reduction. After 40 cycles, a clear transition towards oxidized sulfur species (SO_3^{2-} = 166.8/SO_4^{2-} = 168.8 eV) resulting from electrolyte salt (LiTFSI) decomposition can be observed. An additional peak corresponding to the bridging sulfur atoms in polysulfide chains can also be observed (S^0 = 163.5 eV). After cell failure at 300 cycles, reduced sulfur SEI components are completely eliminated and a huge growth in the intensity of the fully oxidized sulfate species (S^{6+}) can be observed. Based on quantification of the XPS data, the average oxidation number of the sulfur atoms in the lithium interphase increases from -0.67 at 5 cycles to 3.52 at 40 cycles and 5.77 at 300 cycles. Thus, the plating and stripping of lithium in Li-S batteries is accompanied by the decomposition of the electrolyte salt on the lithium surface, with the accumulated decomposition products increasing with cycle number. This agrees with the conclusions drawn from the ToF-SIMS observations in Fig. 2e. Simultaneously, the reduced sulfur SEI components formed during initial cell operation disappear with extended cycling. Reversing this transformation in the composition of the surface interphasial layer could be the key to extending cyclability of lithium-metal anodes in Li-S batteries.

Fig. 3b shows three-dimensional reconstructions of ToF-SIMS depth profiles for the deposited lithium after 5, 40, and 300 cycles. The lateral dimensions of the reconstruction are 100 µm x 100 µm. This provides a visual representation of the spatial distribution for

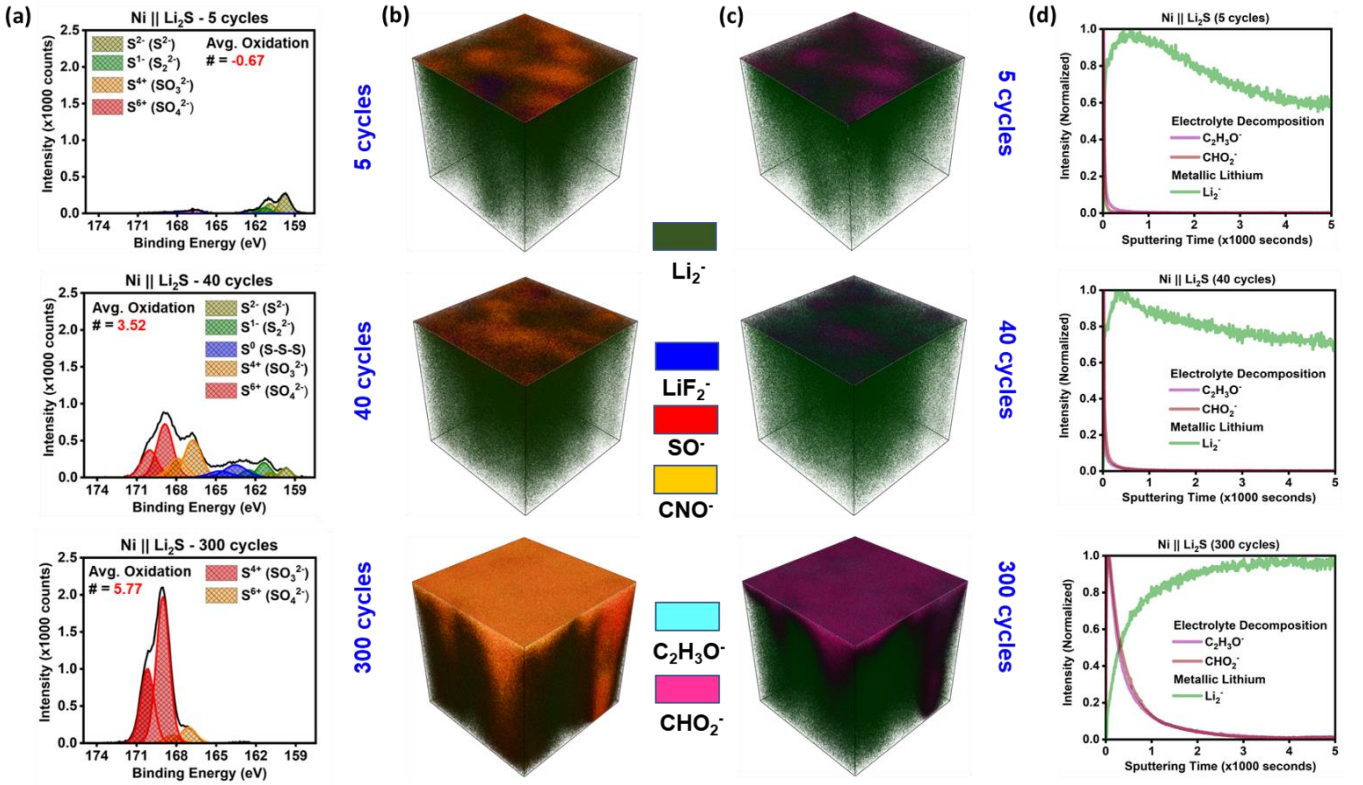

Fig. 3. (a) S 2p spectra obtained with XPS for the deposited lithium in anode-free Ni || Li_2S full cells (cycled at C/10 rate) at 5, 40, and 300 cycles. A clear transition can be observed from reduced sulfur species (Li_2S/Li_2S_2) to oxidized sulfur species (SO_4^{2-}/SO_3^{2-}) with cycling due to the growth of an electrolyte salt decomposition layer. This can also be seen with (b), which shows 3D reconstructions of the ToF-SIMS signal detected for metallic lithium (Li_2^-) and electrolyte salt decomposition products (SO^-, CNO^-, LiF_2^-) at 5, 40, and 300 cycles. (c) Analogous 3D reconstruction of ToF-SIMS signal detected for electrolyte solvent decomposition products – $C_2H_3O^-$ and CHO_2^- secondary ions. The 3D reconstructions allow a visual representation of the various components of the lithium interphase and their spatial distribution. (d) Depth profiles for Li_2^-, $C_2H_3O^-$, and CHO_2^- secondary ions at 5, 40, and 300 cycles. The depth profiles are normalized to the peak intensity for each secondary ion. It can be concluded that long-term cycling of lithium-sulfur batteries is accompanied by the growth of a thick electrolyte decomposition layer on top of the deposited metallic lithium, which renders it electrochemically inactive and leads to failure of the lithium anode.

metallic lithium and various interphasial components. In agreement with the previous data (Fig. 2e), a clear increase in the intensity of SO^-, LiF_2^-, and CNO^- secondary ions, which are concentrated at the surface of the lithium deposit, can be observed at 300 cycles compared to previous cycles. This is in contrast to Li_2^- secondary ions, which remain uniformly distributed throughout the bulk of lithium deposit. The origin of the SO^-, LiF_2^-, and CNO^- secondary ions is attributed to electrolyte salt (LiTFSI and $LiNO_3$) decomposition leading to the formation of $Li_2S_xO_y$, LiF, and RN_xO_y nitrates as interphasial components on lithium surface.[49] In addition to the electrolyte salt, the ether-based electrolyte solvents DOL and DME also reduce on lithium surface to form RCH_2OLi alkoxides, RCO_2Li acetates, and poly-DOL as interphasial components.[50] These species are detected as $C_2H_3O^-$ and CHO_2^- secondary ions in ToF-SIMS analysis of the deposited lithium. Fig. 3c shows three-dimensional reconstructions of the measured ToF-SIMS signal for $C_2H_3O^-$ and CHO_2^- secondary ions at 5, 40, and 300 cycles. A similar trend is observed as in Fig. 3b – decomposition of the ether-based electrolyte solvents on the lithium surface is significantly exacerbated by 300 cycles. Fig. 3d compares depth profiles for $C_2H_3O^-$ and CHO_2^- with that for Li_2^- at 5, 40, and 300 cycles. The depth profiles are scaled from 0 to 1 with respect to the maximum signal intensity. The various electrolyte solvent decomposition products are found to be concentrated at the surface, with the thickness of the interphasial layer growing dramatically by 300 cycles. This closely follows the trend observed in Fig. 2e with the electrolyte salt decomposition layer. Thus, it can be concluded that the long-term cycling of lithium-sulfur batteries engenders the formation of a thick interphasial layer composed of electrolyte decomposition products on the lithium surface. This "traps" the metallic lithium underneath and renders it electrochemically inactive, leading to a depletion of lithium inventory and failure of the lithium anode.

In contrast to electrolyte decomposition products that are concentrated on the lithium surface, certain interphasial components are found throughout the bulk of the deposited lithium. Fig. 4a compares depth profiles for LiO^-, LiS^-, and H^- secondary ions at 5, 40, and 400 cycles. The signal for these secondary ions is more uniformly distributed as a function of sputtering depth and shows some correlation with the depth profiles for Li_2^- secondary ions (shown in Fig. 2d and 2e). LiO^- and LiS^- secondary ions are representative of Li_2O and Li_2S, respectively. Thus, the fully reduced lithium oxides and lithium sulfides are found throughout the bulk of the deposited lithium, and potentially embedded in the porous metallic lithium matrix. H^- secondary ion may be representative of a number of different hydrogen-containing interphasial components. The main sources of hydrogen atoms in the anode-free Ni || Li_2S full cell are the DOL and DME ether-based electrolyte solvents. However, their decomposition products, *i.e.*, RCH_2OLi alkoxides, RCO_2Li acetates, and poly-DOL are only found in the surface interphasial layer (Fig. 3c). Other potential origins of the H^- secondary ion are LiH

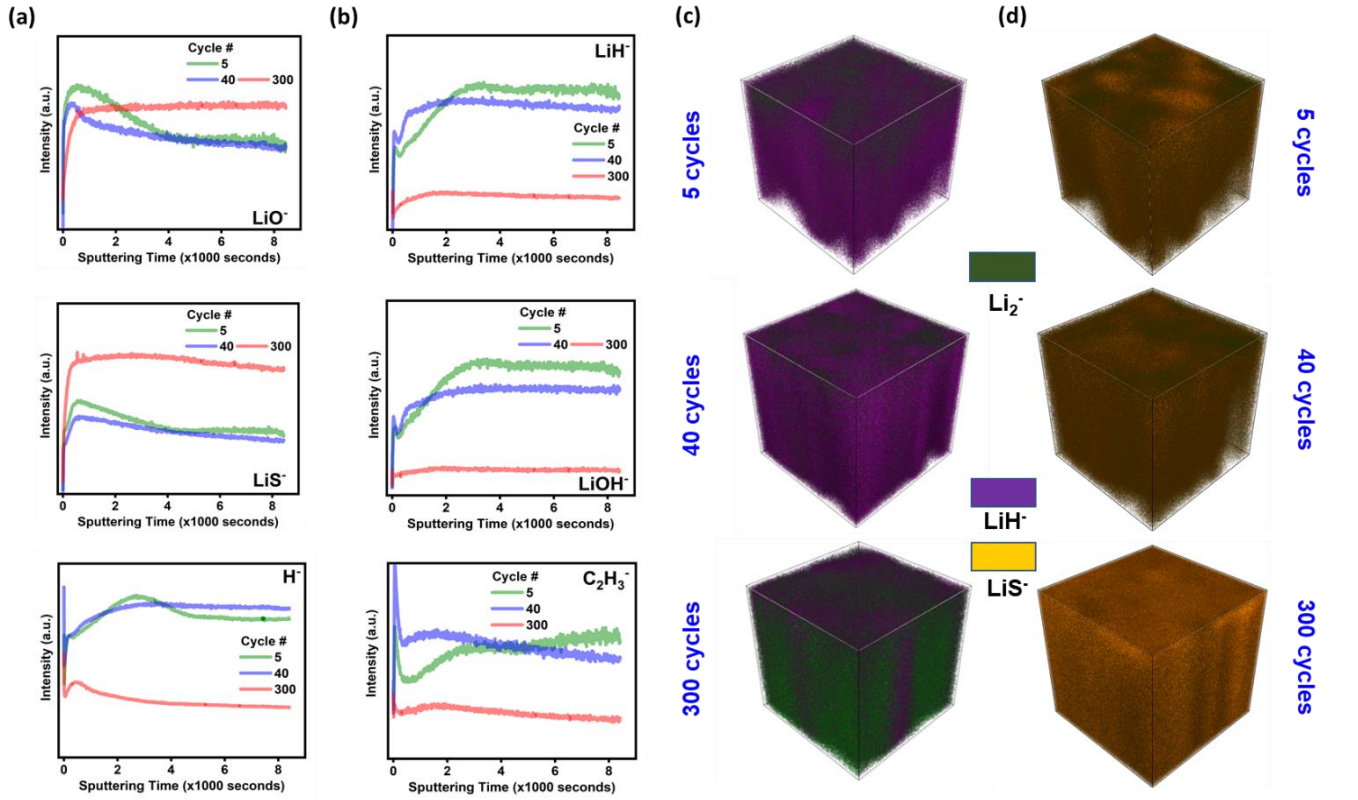

Fig. 4. (a) Depth profiles for LiO^- and LiS^- secondary ions, representative of Li_2O and Li_2S, respectively, and H^- secondary ions, representative of various hydrogen-containing interphasial species, at 5, 40, and 300 cycles. Unlike the electrolyte decomposition products described earlier, these species are present uniformly throughout the deposited lithium. An increase in the concentration of Li_2O and Li_2S in the bulk of deposited lithium is observed with cycling. (b) Depth profiles for different hydrogen-containing secondary ions – LiH^-, representative of LiH, $LiOH^-$, representative of LiOH, and $C_2H_3^-$, representative of various organic interphasial species, at 5, 40, and 300 cycles. A decrease in the concentration of the various hydrogen containing interphasial species is observed with cycling, which indicates substantial gas evolution. These gases include H_2, CH_4, and C_2H_4, and their generation could play a role in the depletion of active lithium inventory. (c) and (d) 3D reconstructions of the ToF-SIMS signal detected for LiH^- and LiS^- at different cycle numbers, showing the decrease in the concentration of LiH and increase in the concentration of Li_2S with cycling.

and LiOH. Fig. 4b compares the depth profiles for LiH^- and $LiOH^-$ secondary ions at 5, 40, and 400 cycles. The close correlation between their depth profiles and that for H^- lends some credence to the possibility of the fully reduced lithium hydride and lithium hydroxide being the main hydrogen-containing interphasial components in the bulk of the deposited lithium.[51] Similar depth profiles are also obtained for LiH_2^- and Li_2H^- secondary ions (Fig. S8), which suggests that a sharp boundary between LiH and lithium metal may not be present. In many studies of the chemistry of lithium-metal anodes, the presence of Li_2O and LiOH is ascribed to the native passivation layer formed on the lithium surface due to exposure to O_2/H_2O impurities in the glovebox ambient.[52,53] However, the deposited lithium in anode-free Ni || Li_2S full cells is formed *in-situ*, and hence any interphasial components detected with ToF-SIMS are also formed *in-situ* during cell operation. Another possible source of hydrogen atoms in the cell is residual moisture in the electrolyte, which forms LiOH in contact with lithium metal.[54,55] The formation of LiH may be understood as one of the complete reduction products of any hydrogen-containing species on the lithium surface. Intriguingly, the depth profile for $C_2H_3^-$ secondary ion (Fig. 4b) is found to follow a similar trend as H^-, with a uniform signal throughout the bulk of the deposited lithium. This is in sharp contrast to the trend for C_2H_3O-, shown in Fig. 3d, which falls off rapidly with increasing depth from the surface. Thus, the decomposition products of the ether-based electrolyte solvents are likely further decomposed in the bulk of the deposited lithium to form various organic (containing C and H) interphasial components.

The signal intensity for LiO^-, LiS^-, and H^- secondary ions does not show an appreciable change during initial cycling from 5 to 40 cycles. However, the signal intensity for LiO^- increases from 40 to 300 cycles, which suggests that the amount of Li_2O in the bulk of the deposited lithium grows during long-term cycling. Simultaneously, the signal intensity for LiS^- secondary ion shows a huge jump from 40 to 300 cycles. Thus, the amount of the reduced sulfur species Li_2S/Li_2S_2 in the bulk of the deposited lithium also increases significantly with cycling, presumably due to extended polysulfide decomposition during long-term cycling. This is the not the trend observed at the surface of the deposited lithium, however, as seen with XPS in Fig. 3a, where the reduced sulfur species are replaced by oxidized sulfur species from electrolyte decomposition. In contrast to both of these cases, the signal intensity for H^- secondary ion, as well as LiH^-, $LiOH^-$, and $C_2H_3^-$ secondary ions, shows a substantial decrease from 40 to 300 cycles. The integrated intensity for H^- at 300 cycles is only ~ 40% of that at 40 cycles. Thus, the hydrogen-containing interphasial components – LiH, LiOH, and any organic species, are mostly depleted from the bulk of the deposited lithium during long-term cycling. One explanation for the depletion of hydrogen-containing species is the significant gas evolution that has been reported in Li-S batteries.[56–58] These gases include H_2, CH_4, C_2H_4, C_2H_6, and H_2S. The main hydrogen-containing interphasial components, LiOH and LiH, are expected to be only metastable during cell operation and can react with residual moisture or electrolyte solvents to evolve H_2 gas.[59] Li_2O is the other main product of the H_2-evolving reactions of LiOH and LiH, and an increase in the signal intensity of LiO^- is observed from 40 to 300 cycles in Fig. 4a. Other hydrocarbon gases are likely evolved due to complete reduction of the organic interphasial components ($C_2H_3^-$) formed by electrolyte solvent decomposition. H_2S gas may be evolved due to reaction between the hydrogen-containing interphasial components and polysulfide species. The evolved gases could get trapped in the bulk of the deposited lithium and rendered unable to escape through the thick surface interphasial layer. The trapped gases would severely limit electrochemical accessibility to the enclosed metallic lithium by blocking off ionic and electronic conduction pathways. Since gas evolution in the bulk of the deposited lithium (inferred from decrease in hydrogen-containing species with ToF-SIMS) is correlated with the depletion of lithium inventory, this could be an additional mechanism that leads to capacity fade in anode-free Ni || Li_2S batteries.

3.4 Effect of Current Density on Interphasial Evolution

In order to confirm these observations about interphasial evolution in Li-S batteries and the proposed mechanisms underlying lithium degradation, a similar analysis with ToF-SIMS was carried out on the deposited lithium in anode-free Ni ||Li_2S full cells cycled at C/5 rate (~ 1 mA cm^{-2}) after 20 and 80 cycles. Fig. 5a shows the integrated intensity for Li_2^- secondary ions, corresponding to the amount of metallic lithium detected over the sampled volume. The intensities are scaled with respect to the total signal intensity for all secondary ions throughout the sputtered depth. Little change in Li_2^- peak intensities is observed from 20 to 80 cycles, although the total peak area between m/z = 14.02 and 14.04 a.u. decreases by 14%. In contrast, the fraction of the initial lithium inventory retained after 20 and 80 cycles at C/5 rate is 54% and 11% respectively (Fig. 5b). As demonstrated previously, there is little correlation between the amount of metallic lithium detected with ToF-SIMS and the amount of electrochemically active lithium inventory retained with cycling. Fig. 5c shows depth profiles for the detected Li_2^- secondary ions at 20 and 80 cycles as a function of sputtering time. The depth profiles are normalized with respect to the total signal for all secondary ions to account for matrix effects. The measured signal intensity at 20 cycles shows a sharp initial peak, but then falls off with increasing depth and settles to a steady value at about 65% of the peak intensity. In contrast, the measured signal intensity at 80 cycles shows a slow increase to a peak value and then falls off gradually to a steady value at about 85% of the peak intensity. This comparative trend in depth profiles for 20 and 80 cycles at C/5 rate is the same observed in Fig. 2d for 5, 40, and 300 cycles at C/10 rate. Thus, the depletion of lithium inventory with cycling in Li-S batteries is attributed to the formation of "dead" or electrochemically inactive metallic lithium (Li^0) as opposed to the loss of lithium to formation of lithium SEI compounds (Li^+) due to side reactions with the electrolyte.

Fig. 5d shows the depth profiles for SO^- and LiF_2^- secondary ions, corresponding to the electrolyte salt (LiTFSI) decomposition products $Li_2S_xO_y$ and LiF, and $C_2H_3O^-$ secondary ions, corresponding to the electrolyte solvent decomposition products RCH_2OLi alkoxides. Each of the electrolyte decomposition products are found to be concentrated on the surface of the deposited lithium with a sharp initial peak in the measured signal intensity that falls off rapidly with increasing sputtering depth. However, the thickness of the surface interphasial layer increases significantly from 20 to 80 cycles. The same trend is observed in Fig. 2e and Fig. 3d when comparing 5, 40, and 300 cycles at C/10 rate. The depth profiles for the various

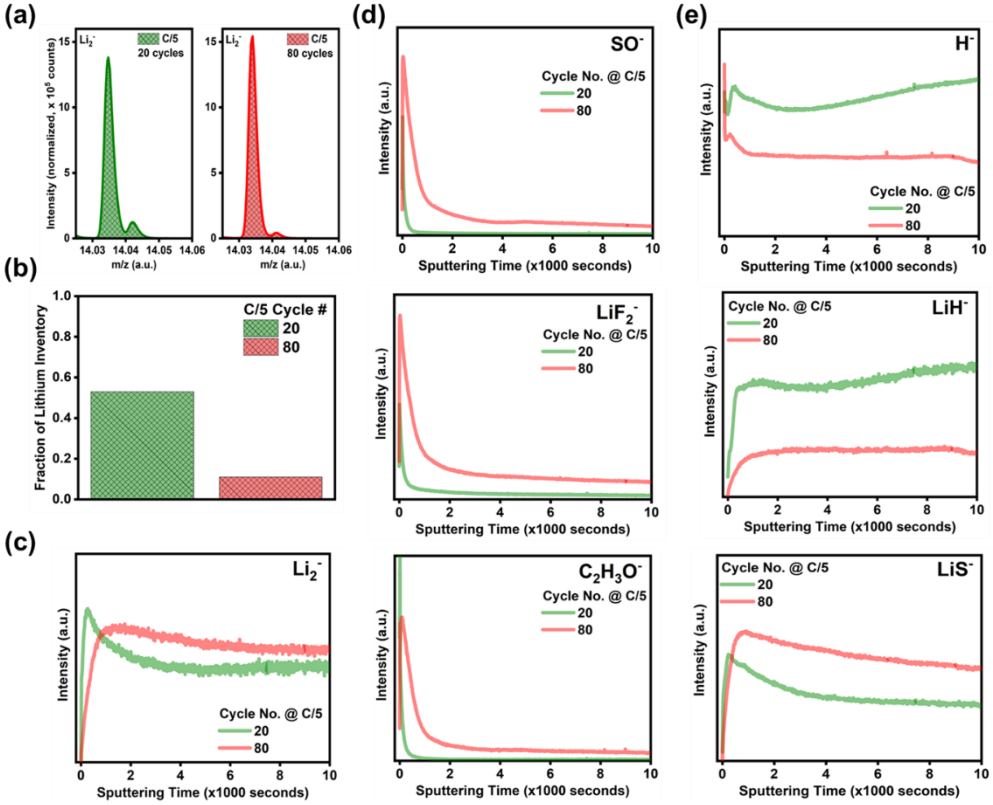

Fig. 5 (a) Integrated intensity of Li_2^- secondary ions for the deposited lithium in anode-free Ni || Li_2S full cells cycled at C/5 rate after 20 and 80 cycles. A significant difference in the total peak area, representative of the amount of metallic lithium detected, is not observed between 20 and 80 cycles. In contrast, a substantial fraction of the initial lithium inventory is depleted between 20 and 80 cycles, as shown in (b). This confirms the observations in Fig. 2 and proves that lithium inventory loss in Li-S batteries is primarily due to the formation of metallic "dead" lithium. (c) Depth profiles for Li_2^- secondary ions as a function of sputtering time at 20 and 80 cycles. (d) Depth profiles for SO^-, LiF_2^-, and $C_2H_3O^-$ secondary ions, indicative of electrolyte decomposition products, at 20 and 80 cycles. The surface interphasial layer composed of electrolyte decomposition products can be observed to grow with cycling. (e) Depth profiles for H^- and LiH^- secondary ions, indicative of various hydrogen-containing interphasial species, and LiS^- secondary ions, indicative of Li_2S, at 20 and 80 cycles. Unlike the electrolyte decomposition products, these species are distributed more uniformly throughout the deposited lithium. A decrease in the concentration of hydrogen-containing interphasial species indicates substantial gas evolution during cell operation, while an increase in the concentration of Li_2S indicates extended polysulfide reduction.

electrolyte decomposition products forms an almost exact inverse of the corresponding depth profile for Li_2^- secondary ions. This suggests that metallic lithium gets covered by a layer of electrolyte decomposition products that increases in thickness with cycling. This blocks electronic and ionic access to the "trapped" metallic lithium and renders it electrochemically inactive. Fig. 2e shows the depth profiles for H^-, LiH^-, and LiS^- secondary ions. Unlike the electrolyte decomposition products described earlier, the fully reduced interphasial components corresponding to H^-, LiH^-, and LiS^- are more uniformly distributed throughout the deposited lithium. The depth profiles for these secondary ions show a relatively steady signal intensity as a function of sputtering time and indicate some correlation with the depth profile for Li_2^- secondary ion. Similar trends are observed as those for 5, 40, and 300 cycles at C/10 rate in Fig. 4a and Fig. 4b. The signal intensity for H^- and LiH^- shows a significant decrease from 20 to 80 cycles. The implied reduction in the amount of the corresponding hydrogen-containing compounds, such as LiH, LiOH, and any organic species, could be indicative of gas generation (H_2, CH_4).[56–58] As described earlier, the evolution of gas molecules due to further decomposition of the hydrogen-containing interphasial components and their entrapment in the bulk of the deposited lithium can block electronic and ionic access to adjacent metallic lithium. Simultaneously, the amount of reduced sulfur species (Li_2S, Li_2S_2) in the bulk of the deposited lithium increases from 20 to 80 cycles. This can also play a role in passivating the metallic lithium surface and have a detrimental effect on its electrochemical activity.

As shown in Fig. 1d and Fig. 1e, an increase in the applied current density from C/10 (~ 0.5 mA cm^{-2}) to C/5 (~ 1 mA cm^{-2}) brings about a three-fold increase in the lithium inventory loss rates, from 0.6% per cycle to 1.8% per cycle. The faster lithium inventory loss at C/5 is shown here to be accompanied by a similar interphasial evolution with cycling as observed previously at C/10 rate. A significant amount of metallic lithium is still detected even as most of the lithium inventory is depleted at 80 cycles. Its depletion is attributed to the formation and growth of a thick surface interphasial layer composed of electrolyte decomposition products. Additional interphasial changes in the bulk of the deposited lithium, including evolution of various hydrogen-containing gases and growth of sulfide-rich interphases could also play a role in accelerating lithium degradation with cycling. As explained earlier, higher applied current densities exacerbate the high-surface area mossy deposition of lithium, engenders even more severe parasitic side reactions with the electrolyte, and increase lithium inventory loss rates. Hence, the advanced stages of interphasial evolution are observed at 80 cycles for C/5 rate compared to 300 cycles for C/10 rate.

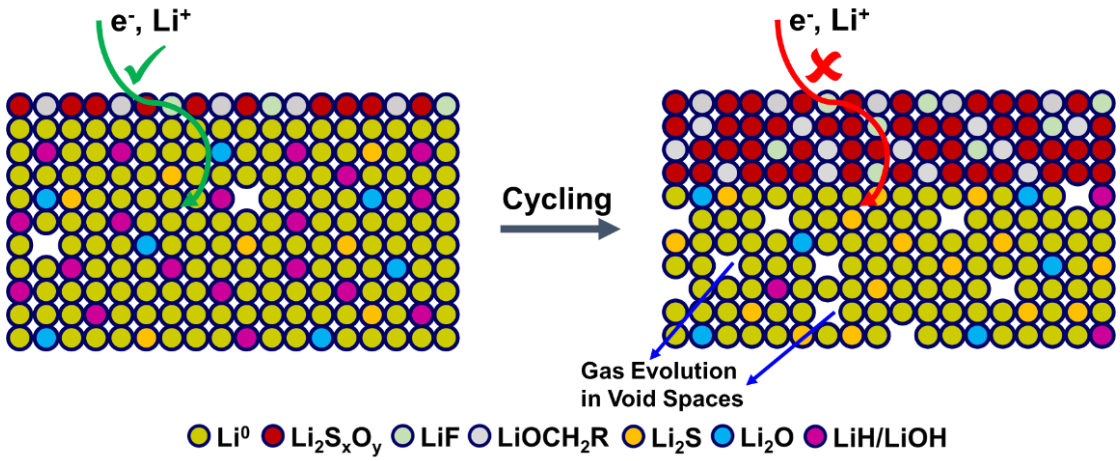

Fig. 6 Lithium degradation in Li-S batteries with cycling. In the initial stages of cycling, the deposited lithium is covered by a thin surface interphasial layer composed of partially reduced electrolyte decomposition products. The bulk is composed of fully-reduced interphasial species such as Li_2O, Li_2S, LiH, LiOH, and other organic species. The metallic lithium is electrochemically active due to facile ionic access through the surface interphasial layer. In the advanced stages of cycling, the surface interphasial layer grows significantly in thickness, which blocks ionic access to the metallic lithium and renders it electrochemically inactive. The deposited lithium also increases in porosity due to the substantial volume changes that occur with cycling. The concentration of various hydrogen-containing interphasial species decreases with cycling, indicating considerable gas evolution in the void spaces of the deposited lithium. The concentration of Li_2S in the bulk of the deposited lithium also increases with cycling due to extended polysulfide reduction.

3.5 Degradation of Lithium in Li-S Batteries

The ToF-SIMS experiments show that the deposited lithium in the anode-free Ni || Li_2S full cell possesses a bilayer structure, with a layer of electrolyte decomposition products forming the top interphase and the bulk made up of metallic lithium and other interphasial components, such as Li_2O, Li_2S, LiH, and LiOH. The surface interphasial layer is composed of various inorganic electrolyte-salt (LiTFSI/$LiNO_3$) decomposition products and polymeric or organic electrolyte-solvent (DOL/DME) decomposition products. These surface interphasial components, such as $Li_2S_xO_y$ and RCO_2Li, are only partially reduced due to insufficient electron conduction pathways and limited access to metallic lithium at the surface. In contrast, the bulk interphasial components are fully reduced due to facile access to metallic lithium and abundant electron conduction pathways. The deposited lithium also adopts a porous three-dimensional structure with high surface area due to the mossy growth mechanism, and the deposition morphology only degrades further with cycling. This is confirmed by the SEM images of the top surface of the deposited lithium in Li || Li_2S half cells and Ni || Li_2S full cells after 5 and 50 cycles at C/5 rate (Fig. S10). Cross-sectional images of the deposited lithium show the growth in thickness from ~ 50 µm to ~ 80 µm in the Ni || Li_2S full cell, indicating a substantial increase in porosity with cycling (Fig. S11). Furthermore, since lithium metal is a "hostless" anode, a substantial fraction of the deposited lithium is eliminated and reconstructed during discharge and charge, respectively. This induces severe volume changes with cycling. The large surface area of the deposited lithium combined with its reconstruction during every cycle intensifies parasitic side reactions with the electrolyte. Despite the severity of these side reactions, metallic lithium is found to remain mostly intact through cycling. The side reactions are self-limiting, i.e. the initial formation of an interphasial layer impedes electron transfer from lithium metal to the electrolyte, which impedes further interphasial growth.[60] While there is no significant consumption of metallic lithium in the side reactions, it is still rendered electrochemically inaccessible due to the structural and compositional evolution of interphases in the deposited lithium. The electrolyte decomposition products do not form a uniform layer on the top surface. This layer varies in thickness and composition in certain parts of the surface compared to others. Simultaneously, the metallic lithium underneath does not assemble into a dense and homogenous bulk but instead forms isolated pockets due to the porosity of the deposited lithium. The number of effective ionic transport pathways into the metallic lithium in the bulk dwindle as the electrolyte decomposition layer (*e.g.*, $Li_2S_xO_y$ and RCO_2Li) grows in thickness with cycling. This traps the metallic lithium underneath as some of the isolated pockets of metallic lithium in the bulk lose access to Li^+ ions and electrons and are rendered "dead". In addition, a combination of gas (e.g., H_2, C_2H_4) evolution in the bulk of the deposited lithium as well as an increase in the concentration of Li_2O and Li_2S limits ionic and electronic conduction pathways to the enclosed lithium metal. These mechanisms underlying interphasial evolution in the deposited lithium work in concert to render metallic lithium electrochemically inaccessible and engender the rapid depletion of lithium inventory. These mechanisms are also likely to be applicable under lean-electrolyte conditions. Based on the results obtained in this work, Fig. 6 illustrates the interphasial evolution accompanying lithium degradation in Li-S batteries.

4 Conclusions

In order to realize practically viable lithium-sulfur batteries with thin lithium foils, the poor efficiency of cycling lithium metal in liquid electrolytes needs to be addressed. The consequent rapid depletion of lithium inventory leads to poor cyclability, or conversely, the need to employ excess lithium to maintain cyclability at the expense of energy density. An accurate understanding of lithium degradation in Li-S batteries is necessary to meet the challenge of maintaining cyclability under practically relevant lithium-limited conditions. Anode-free Ni || Li_2S full cells, with the lithium to sulfur capacity ratio equal to 1, provide a useful framework for evaluating lithium deposition in Li-S batteries. By using a limited lithium inventory to constrain cycle life, anode-free full cells enable the most realistic

assessment of electrochemical performance. Identification of the lithium-limited cycling regime in anode-free full cells can be used to derive a quantitative estimate of the lithium inventory loss rate per cycle. This parameter provides a robust and accurate evaluation of lithium degradation in Li-S batteries. Unlike Coulombic efficiency, the lithium inventory loss rate is a more reliable predictor of cycle life under practically relevant and constrained cell design and testing conditions. It also enables an effective comparison of lithium degradation across different lithium-limited systems. This framework of using anode-free full cells to quantitatively estimate lithium inventory loss rates can be facilely extended to evaluating lithium deposition in conjunction with other cathodes as well.

In this work, sulfur and lithium inventory loss rates are calculated by deconvoluting the sulfur-limited and lithium-limited regimes in the cycling of anode-free Ni || Li_2S full cells. It is found that while the Li_2S cathode suffers from a high capacity fade during the first 5 cycles, its subsequent inventory loss rate (0.2% per cycle at C/10 rate) is much less compared to that for lithium (0.6% per cycle at C/10 rate). Doubling the C-rate increases the sulfur inventory loss rate to only 0.3% per cycle but triples the lithium inventory loss rate to 1.8% per cycle. Thus, lithium degradation is the main factor constraining long term cyclability of Li-S batteries. The deposited lithium in anode-free Ni || Li_2S full cells also makes an excellent template for characterizing the evolution of lithium interphases in Li-S batteries. By careful analysis with ToF-SIMS, significant amounts of metallic lithium were detected even as most of the lithium inventory was depleted in the advanced stages of cycling. Thus, the depletion of lithium inventory in Li-S batteries can be primarily attributed to the formation of electrochemically inaccessible metallic "dead" lithium as opposed to the loss of lithium in parasitic side reactions with the electrolyte to form lithium SEI compounds. The plating and stripping of lithium is accompanied with the formation and growth of a thick electrolyte decomposition layer on the lithium surface, which impedes electronic and ionic access to the metallic lithium trapped underneath. The loss of lithium inventory is also correlated with the disappearance of hydrogen-containing interphasial species in the bulk of the deposited lithium. This indicates that the cycling of lithium metal is concomitant with considerable gas evolution, particularly H_2, CH_4, and C_2H_4. This can have a further detrimental effect on the electrochemical activity of the trapped metallic lithium, especially if the gases are trapped in void spaces in the porous lithium deposit.

Further work on improving the cyclability of Li-S batteries operating under stringent cell design and testing conditions need to be focused on reducing the lithium inventory loss rate, as measured using the anode-free full cell configuration. For certain applications, the cyclability requirements for Li-S batteries may be flexible given their high energy density. Nevertheless, a lithium inventory loss rate less than 0.1% per cycle is necessary for commercial application, with a reversible capacity greater than 4 mAh cm^{-2} and a current density greater than 2 mA cm^{-2}. Based on the results in this work, devising electrolyte formulations that show reduced decomposition on the lithium surface might repress the rapid depletion of lithium inventory. The use of various electrolyte additives in addition to $LiNO_3$ or even modifications to the LiTFSI electrolyte salt might prove helpful in this regard. As a useful corollary, reduced electrolyte decomposition can also enable cell operation under lean-electrolyte conditions, as the limited electrolyte amount can be utilized for a longer number of cycles. Optimized electrolytes may also help suppress the substantial gas generation that occurs during cell operation. Gas evolution in Li-S batteries and its effect on lithium cycling efficiency remains a significantly under-explored area of research in the community. It is hoped that the framework demonstrated in this work and the insights generated into inventory depletion and interphasial evolution in Li-S batteries could prove useful for efforts towards definitively reducing lithium inventory losses in Li-S batteries.

Conflicts of interest

There are no conflicts to declare.

Acknowledgements

This work was supported by the Assistant Secretary for Energy Efficiency and Renewable Energy, Office of Vehicle Technologies of the U.S. Department of Energy through the Advanced Battery Materials Research (BMR) Program (Battery500 Consortium) award number DE-EE0007762.

References

1 A. Manthiram, S.-H. Chung and C. Zu, *Adv. Mater.*, 2015, **27**, 1980–2006.
2 A. Manthiram, Y. Fu, S.-H. Chung, C. Zu and Y.-S. Su, *Chem. Rev.*, 2014, **114**, 11751–11787.
3 J. He and A. Manthiram, *Energy Storage Mater.*, 2019, **20**, 55–70.
4 S. Chung and A. Manthiram, *Adv. Mater.*, 2019, **31**, 1901125.
5 S.-H. Chung, C.-H. Chang and A. Manthiram, *Adv. Funct. Mater.*, 2018, **28**, 1801188.
6 S. H. Chung and A. Manthiram, *Joule*, 2018, **2**, 710–724.
7 A. Bhargav, J. He, A. Gupta and A. Manthiram, *Joule*, 2020, **4**, 285–291.
8 W. Xu, J. Wang, F. Ding, X. Chen, E. Nasybulin, Y. Zhang and J.-G. Zhang, *Energy Environ. Sci.*, 2014, **7**, 513–537.
9 D. Lin, Y. Liu and Y. Cui, *Nat. Nanotechnol.*, 2017, **12**, 194–206.
10 P. Bai, J. Li, F. R. Brushett and M. Z. Bazant, *Energy Environ. Sci.*, 2016, **9**, 3221–3229.
11 S. Chen, C. Niu, H. Lee, Q. Li, L. Yu, W. Xu, J. G. Zhang, E. J. Dufek, M. S. Whittingham, S. Meng, J. Xiao and J. Liu, *Joule*, 2019, **3**, 1094–1105.
12 J. Liu, Z. Bao, Y. Cui, E. J. Dufek, J. B. Goodenough, P. Khalifah, Q. Li, B. Y. Liaw, P. Liu, A. Manthiram, Y. S. Meng, V. R. Subramanian, M. F. Toney, V. V. Viswanathan, M. S. Whittingham, J. Xiao, W. Xu, J. Yang, X. Q. Yang and J. G. Zhang, *Nat. Energy*, 2019, **4**, 180–186.
13 J. Xiang, L. Yang, L. Yuan, K. Yuan, Y. Zhang, Y. Huang, J. Lin, F. Pan and Y. Huang, *Joule*, 2019, **3**, 2334–2363.
14 C. Fang, X. Wang and Y. S. Meng, *Trends Chem.*, 2019, **1**, 152–158.
15 J. Xiao, *Science*, 2019, **366**, 426–427.

16 X.-B. Cheng, C. Yan, J.-Q. Huang, P. Li, L. Zhu, L. Zhao, Y. Zhang, W. Zhu, S.-T. Yang and Q. Zhang, *Energy Storage Mater.*, 2017, **6**, 18–25.

17 M. Hagen, P. Fanz and J. Tübke, *J. Power Sources*, 2014, **264**, 30–34.

18 X.-B. Cheng, C. Yan, H.-J. Peng, J.-Q. Huang, S.-T. Yang and Q. Zhang, *Energy Storage Mater.*, 2018, **10**, 199–205.

19 C.-Z. Zhao, X.-B. Cheng, R. Zhang, H.-J. Peng, J.-Q. Huang, R. Ran, Z.-H. Huang, F. Wei and Q. Zhang, *Energy Storage Mater.*, 2016, **3**, 77–84.

20 W. Li, H. Yao, K. Yan, G. Zheng, Z. Liang, Y.-M. Chiang and Y. Cui, *Nat. Commun.*, 2015, **6**, 7436.

21 E. C. Miller, R. M. Kasse, K. N. Heath, B. R. Perdue and M. F. Toney, *J. Electrochem. Soc.*, 2018, **165**, A6043–A6050.

22 X. Yu and A. Manthiram, *Energy Environ. Sci.*, 2018, **11**, 527–543.

23 X. Yu and A. Manthiram, *Acc. Chem. Res.*, 2017, **50**, 2653–2660.

24 M. Winter, *Zeitschrift fur Phys. Chemie*, 2009, **223**, 1395–1406.

25 E. Peled and S. Menkin, *J. Electrochem. Soc.*, 2017, **164**, A1703–A1719.

26 S. Li, M. Jiang, Y. Xie, H. Xu, J. Jia and J. Li, *Adv. Mater.*, 2018, **30**, 1706375.

27 Y. Zhao, K. R. Adair and X. Sun, *Energy Environ. Sci.*, 2018, **11**, 2673–2695.

28 P. Shi, X. Q. Zhang, X. Shen, R. Zhang, H. Liu and Q. Zhang, *Adv. Mater. Technol.*, 2020, **5**, 1900806.

29 C. Zu, N. Azimi, Z. Zhang and A. Manthiram, *J. Mater. Chem. A*, 2015, **3**, 14864–14870.

30 C. Zu, A. Dolocan, P. Xiao, S. Stauffer, G. Henkelman and A. Manthiram, *Adv. Energy Mater.*, 2016, **6**, 1501933.

31 X. B. Cheng, R. Zhang, C. Z. Zhao and Q. Zhang, *Chem. Rev.*, 2017, **117**, 10403–10473.

32 C. Yan, X. Q. Zhang, J. Q. Huang, Q. Liu and Q. Zhang, *Trends Chem.*, 2019, **1**, 693–704.

33 X.-B. Cheng, J.-Q. Huang and Q. Zhang, *J. Electrochem. Soc.*, 2018, **165**, A6058–A6072.

34 J. Qian, B. D. Adams, J. Zheng, W. Xu, W. A. Henderson, J. Wang, M. E. Bowden, S. Xu, J. Hu and J.-G. Zhang, *Adv. Funct. Mater.*, 2016, **26**, 7094–7102.

35 J. G. Zhang, *Nat. Energy*, 2019, **4**, 637–638.

36 S. Nanda, A. Gupta and A. Manthiram, *Adv. Energy Mater.*, 2018, **8**, 1801556.

37 D. Zheng, X.-Q. Yang and D. Qu, *ChemSusChem*, 2016, **9**, 2348–2350.

38 W. Li, U. H. Kim, A. Dolocan, Y. K. Sun and A. Manthiram, *ACS Nano*, 2017, **11**, 5853–5863.

39 W. Li, E. M. Erickson and A. Manthiram, *Nat. Energy*, 2020, **5**, 26–34.

40 Y. Yang, Y. Liu, Z. Song, Y. Zhou and H. Zhan, *ACS Appl. Mater. Interfaces*, 2017, **9**, 38950–38958.

41 S. Zhang, K. Zhao, T. Zhu and J. Li, *Prog. Mater. Sci.*, 2017, **89**, 479–521.

42 J. Xu, R. D. Deshpande, J. Pan, Y.-T. Cheng and V. S. Battaglia, *J. Electrochem. Soc.*, 2015, **162**, A2026–A2035.

43 R. N. S. Sodhi, *Analyst*, 2004, **129**, 483–487.

44 Z. Wang, B. Liu, E. W. Zhao, K. Jin, Y. Du, J. J. Neeway, J. V. Ryan, D. Hu, K. H. L. Zhang, M. Hong, S. Le Guernic, S. Thevuthasan, F. Wang and Z. Zhu, *J. Am. Soc. Mass Spectrom.*, 2015, **26**, 1283–1290.

45 C. Fang, J. Li, M. Zhang, Y. Zhang, F. Yang, J. Z. Lee, M.-H. Lee, J. Alvarado, M. A. Schroeder, Y. Yang, B. Lu, N. Williams, M. Ceja, L. Yang, M. Cai, J. Gu, K. Xu, X. Wang and Y. S. Meng, *Nature*, 2019, **572**, 511–515.

46 M. L. Meyerson, J. K. Sheavly, A. Dolocan, M. P. Griffin, A. H. Pandit, R. Rodriguez, R. M. Stephens, D. A. Vanden Bout, A. Heller and C. B. Mullins, *J. Mater. Chem. A*, 2019, **7**, 14882–14894.

47 C. Zu and A. Manthiram, *J. Phys. Chem. Lett.*, 2014, **5**, 2522–2527.

48 J. Li and A. Manthiram, *Adv. Energy Mater.*, 2019, **9**, 1902731.

49 Z. L. Brown, S. Jurng and B. L. Lucht, *J. Electrochem. Soc.*, 2017, **164**, A2186–A2189.

50 C. Fiedler, B. Luerssen, M. Rohnke, J. Sann and J. Janek, *J. Electrochem. Soc.*, 2017, **164**, A3742–A3749.

51 M. J. Zachman, Z. Tu, S. Choudhury, L. A. Archer and L. F. Kourkoutis, *Nature*, 2018, **560**, 345–349.

52 K. Wang, *J. Electrochem. Soc.*, 1996, **143**, 422.

53 G. Zhuang, *J. Electrochem. Soc.*, 1998, **145**, 159.

54 M. H. Cho, J. Trottier, C. Gagnon, P. Hovington, D. Clément, A. Vijh, C. S. Kim, A. Guerfi, R. Black, L. Nazar and K. Zaghib, *J. Power Sources*, 2014, **268**, 565–574.

55 N. Togasaki, T. Momma and T. Osaka, *J. Power Sources*, 2014, **261**, 23–27.

56 H. Schneider, T. Weiß, C. Scordilis-Kelley, J. Maeyer, K. Leitner, H. J. Peng, R. Schmidt and J. Tomforde, *Electrochim. Acta*, 2017, **243**, 26–32.

57 A. Jozwiuk, B. B. Berkes, T. Weiß, H. Sommer, J. Janek and T. Brezesinski, *Energy Environ. Sci.*, 2016, **9**, 2603–2608.

58 X. Chen, T. Z. Hou, B. Li, C. Yan, L. Zhu, C. Guan, X. B. Cheng, H. J. Peng, J. Q. Huang and Q. Zhang, *Energy Storage Mater.*, 2017, **8**, 194–201.

59 D. Aurbach and I. Weissman, *Electrochem. commun.*, 1999, **1**, 324–331.

60 A. Wang, S. Kadam, H. Li, S. Shi and Y. Qi, *npj Comput. Mater.*, 2018, **4**, 1-26